



Ohmic resistance in zero gap alkaline electrolysis with a Zirfon diaphragm

Matheus T. de Groot^{a,b,*}, Albertus W. Vreman^{a,b}

^a Eindhoven University of Technology, P.O. Box 513, 5600 MB Eindhoven, the Netherlands

^b Nouryon Industrial Chemicals, P.O. Box 75730, 3811 LP Amersfoort, the Netherlands



ARTICLE INFO

Article history:

Received 28 October 2020

Revised 23 December 2020

Accepted 23 December 2020

Available online 28 December 2020

Keywords:

Alkaline water electrolysis

Area resistance

Zero gap configuration

Secondary current distribution modeling

ABSTRACT

Alkaline water electrolyzers are traditionally operated at low current densities, due to high internal ohmic resistance. Modern diaphragms with low internal resistance such as the Zirfon diaphragm combined with a zero gap configuration potentially open the way to operation at higher current densities. Data for the Zirfon diaphragm show that the resistance is only 0.1–0.15 $\Omega \text{ cm}^2$ in 30% KOH at 80 °C, in line with estimations based on the porosity. Nevertheless, an analysis of data on zero gap alkaline electrolyzers with Zirfon reveals that the area resistances are significantly higher, ranging from 0.23 to 0.76 $\Omega \text{ cm}^2$. A numerical simulation of the secondary current distribution in the zero gap configuration shows that an uneven current distribution, imperfect zero gap and the presence of bubbles can probably only partly explain the increased resistance. Therefore, other factors such as the presence of nanobubbles could play a role.

© 2021 The Authors. Published by Elsevier Ltd.

This is an open access article under the CC BY license (<http://creativecommons.org/licenses/by/4.0/>)

1. Introduction

Renewable hydrogen produced by water electrolysis is expected to play a key role in the energy transition. Of the available water electrolysis technologies alkaline water electrolysis is currently the most cost-effective, combining low capital costs with a good efficiency [1–3]. This is related to the fact that alkaline electrolyzers are mostly made of cheap materials such as nickel plated steel [4, 5] and do not require expensive noble metals or membranes. Yet, alkaline electrolyzers also suffer from disadvantages, most notably the fact that to be efficient they typically need to be operated at low current density ($\sim 0.2 \text{ A/cm}^2$) [4]. As a result alkaline electrolyzers are much bulkier and heavier than PEM electrolyzers that operate at much higher current densities. This means that alkaline water electrolysis plants require larger buildings and heavier foundations adding to the total capital costs.

In order to improve the cost-competitiveness of alkaline technology it would be attractive if the current density of the technology could be increased without decreasing the efficiency. This requires a combination of electrode materials with low overpotentials and a cell design with minimal area resistance. During most of the twentieth century this was not possible, since thick asbestos

diaphragms of 4 mm with a resistance of $\sim 1.0 \Omega \text{ cm}^2$ were used to separate the catholyte from the anolyte [4]. The high area resistance of the separator meant that an increase in current density would be accompanied by a large increase in cell potential. At that time there was no alternative porous material that was sufficiently stable in the 25–35 wt% KOH electrolyte. Additionally, the use of asbestos limited the operating temperature to a maximum of 90 °C [6], making it impossible to benefit from increased conductivity at higher temperature.

In the last two decades of the twentieth century the search started for more conductive alternatives to asbestos, which was accelerated by the fact that asbestos needed to be phased due to health risks. A wide range of new materials was investigated, including nickel oxide, PTFE and different types of polysulfone [7]. One of the materials that has been commercialized is Zirfon® Perl UTP 500 (Zirfon), which consists of a combination of zirconium oxide and polysulfone and combines good conductivity with a high bubble point and good wettability [6, 8] giving it the right properties to act as a gas separation diaphragm. The thickness of Zirfon is 0.5 mm and its resistance in 30 wt% KOH was reported to be 0.3 $\Omega \text{ cm}^2$ at 20 °C and 0.13 $\Omega \text{ cm}^2$ at 80 °C [9]. The reported conductivity of Zirfon is comparable to the conductivity reported for Nafion membranes used in PEM water electrolysis [10] and hence it should be a good basis for a high current density alkaline electrolyzer with a good efficiency.

* Corresponding author at: Eindhoven University of Technology, P.O. Box 513, 5600 MB Eindhoven, the Netherlands.

E-mail address: M.T.d.Groot@tue.nl (M.T. de Groot).

Other important ingredients for a high current density alkaline electrolyzer are the anode and cathode materials. The scientific literature on electrocatalysts for hydrogen and oxygen evolution in alkaline media is extensive, yet work under industrially relevant conditions ($>70\text{ }^\circ\text{C}$, $> 0.2\text{ A/cm}^2$, 30% KOH) is more limited [11]. Under these conditions good anode materials are typically high surface area nickel materials, resulting in overpotentials of 230–300 mV at 0.1 A/cm^2 and $90\text{ }^\circ\text{C}$ with a Tafel slope of 50–60 mV [12]. For the cathode materials learnings can be taken from developments in the chlor-alkali industry [13], where cathodic conditions are very similar to alkaline water electrolysis (32 wt% NaOH versus 30 wt% KOH). Using noble metal based coatings with a.o. ruthenium oxide or platinum overpotentials of lower than 80 mV at 0.6 A/cm^2 and $90\text{ }^\circ\text{C}$ can be reached, whereas with Raney-Ni type materials overpotentials are around 120 mV at 0.6 A/cm^2 [14, 15]. For both materials Tafel slopes of 40–60 mV are observed [13]. It is an economic trade-off whether the savings related to the lower overpotentials outweigh the extra costs associated with the use of noble metals. Given the scarcity of some of these noble metals it would be preferred if their use can be avoided for the expected large-scale deployment of water electrolysis.

The last prerequisite for a high current density alkaline electrolyzer is a good “zero gap” configuration. “Zero gap” means that the electrodes are pushed against the diaphragm to minimize the area resistance through the solution. The zero gap consists of a complex interplay of ion transport, kinetics, bubbles and supersaturation. The zero gap concept for alkaline electrolyzers was already applied in the fifties of the last century in the Zdansky–Lonza design [16]. Yet, zero gap designs have been developed in an empirical way and fundamental research in this area for alkaline water electrolysis is limited [17, 18]. We lack a good understanding on the performance of zero gap configurations and on their ability to minimize area resistance. More research in this area is needed to come to the most optimal 3D-electrode structures for alkaline water electrolysis.

Based on the above it seems all ingredients for a high current density alkaline electrolyzer are present. Combining the Zirfon diaphragm with high surface area Raney-Ni electrodes in a zero gap configuration should result in a good electrolyzer performance. With a back-of-the-envelope calculation employing the diaphragm conductivity, electrode overpotentials and the reversible potential of $\sim 1.15\text{ V}$ at $90\text{ }^\circ\text{C}$ [19] one can estimate the cell potential to be around $1.65\text{--}1.70\text{ V}$ at 0.6 A/cm^2 (at atmospheric pressure). Indeed, already in 1998 Vermeiren reported a cell potential of 1.67 V at 0.8 A/cm^2 and $90\text{ }^\circ\text{C}$ when Zirfon was used in combination with vacuum plasma-sprayed (VPS) electrodes [9].

However, more recent papers using a Zirfon diaphragm in combination with a zero gap configuration have been unable to meet the same performance as Vermeiren, even though a number of these papers also make use of high surface area Raney-Ni electrodes [17, 20–25]. The paper with the best performance only reaches a cell potential of 1.9 V at 1 A/cm^2 and $80\text{ }^\circ\text{C}$ in 30% KOH [21]. A closer look at the papers reveals that the main reason for this poorer performance is a relatively high area resistance of over $0.3\text{ }\Omega\text{ cm}^2$ in 30% KOH at $80\text{ }^\circ\text{C}$ as determined with impedance spectroscopy [21, 23]. This is over a factor two higher than the previously mentioned diaphragm resistance of $0.13\text{ }\Omega\text{ cm}^2$.

There are multiple possible reasons for this apparent discrepancy in area resistance in zero gap electrolyzers with the Zirfon diaphragm. They include a higher actual resistivity of present-day Zirfon or a significant resistance outside the diaphragm, e.g. caused by bubbles. It is the purpose of this study to build a better understanding of the area resistance in zero gap alkaline electrolyzers and in this way accelerate the development of high current density alkaline electrolyzers. We do this by assessing diaphragm resistance, analyzing current–voltage-relations and impedance re-

Table 1
Properties of the Zirfon® Perl UTP 500 diaphragm [28, 49].

Property	Value
Thickness (μm)	500 ± 50
Porosity (%)	$50^a \pm 10$
Pore size (μm)	0.15 ± 0.05
Bubble point (bar)	2 ± 1

^a A value of 55% has also been reported [49].

sults and calculating expected ohmic losses in zero gap configurations.

2. Methods

2.1. Analysis of diaphragm conductivity

Table 1 lists properties of the Zirfon separator relevant for our analysis. The Zirfon separator is not an ion-selective membrane, but a porous diaphragm with relatively large pores of 150 nm. It does not contain any charged groups and hence the conductivity of the separator is determined by the electrolyte that fills the pores. The resistivity of the diaphragm R is related to the resistivity of the electrolyte R_0 via the MacMullin number N_m [26] as shown in Eq. (1). This MacMullin number depends on the porosity ε and tortuosity factor τ^2 (not to be confused with the tortuosity [27]) of the porous medium. The porosity of the Zirfon separator has been reported to be $50 \pm 10\%$ [28]. The tortuosity factor depends on the structure and configuration of the porous network nature. Although some investigations have been carried out on the structure of Zirfon [8, 6, 29], no attempt has been made to determine the tortuosity factor. Therefore, we can only make an estimate of the tortuosity factor and the corresponding MacMullin number based on general correlations that relate the tortuosity factor to the porosity [30]. The best known is Eq. (2), which is Bruggeman's equation for a porous medium consisting of spheres [31]. In this equation the tortuosity factor κ is equal to the inverse square root of the porosity. For a porosity of 50% this corresponds to a MacMullin number of 2.8. Bruggeman has also made an equation for a porous medium consisting of cylinders, in which the tortuosity factor is equal to the inverse of the porosity [31], which results in a MacMullin number of 4. Other correlations for the MacMullin number suggest numbers ranging from 2.5 to 3.8 for a porosity of 50% [27, 30]. Therefore, the Zirfon separator is expected to have a MacMullin number in the range of 2.6 to 4.0.

$$N_m = \frac{R}{R_0} = \frac{\tau^2}{\varepsilon} \quad (1)$$

$$\tau^2 = \varepsilon^{-0.5} \quad (2)$$

The electrolyte used in alkaline water electrolysis is typically KOH. Its conductivity κ can be modeled using Eq. (3), in which M is the molarity in mol/l and T is the temperature in Kelvin [32]. Some investigations instead use NaOH as electrolyte, which is somewhat less conductive [13].

$$\kappa = -2.04M - 2.8 \cdot 10^{-3}M^2 + 5.33 \cdot 10^{-3}MT + 207 \frac{M}{T} + 1.04 \cdot 10^{-3}M^3 - 3 \cdot 10^{-7}M^2T^2 \quad (3)$$

The Zirfon separator also contains an open mesh-fabric support structure, which is not porous. From an image of the separator in [28] the diameter of the threads is estimated to be $100\text{ }\mu\text{m}$ with an interthread distance of $500\text{ }\mu\text{m}$. Through the threads no ion flow is possible, which means that the ion flow through the porous part is somewhat higher than the geometric current density, resulting in a higher potential drop. In our estimation of the

Table 2
Electrode materials of current–voltage datasets used in this work.

Reference	Electrode area (cm ²)	Anode	Anode coating	Cathode	Cathode coating
Vermeiren [9, 8]	250	unknown	VPS NiAl/Co ₃ O ₄	unknown	VPS NiAl/Mo
Bowen [25]	300	unknown	None or VPS NiAl	unknown	None or VPS Ni Al
Ju [20]	20	Ni trapezoidal prism	None	Ni Trapezoidal prism	none
Baumgart [24]	2711	Ni Perforated plate	None	Ni Perforated plate	Raney Ni
Schalenbach [21]	25	Perforated plate	VPS NiAl	Perforated plate	VPS NiAl/Mo
Kraglund [22]	25	Ni perforated plate	None or Raney Ni	Ni foam	None or Raney NiMo
Phillips [17]	10	Stainless steel mesh	None	Stainless steel mesh	none
Fischer [38]	4360	Ni perforated plate	None	Ni perforated plate	Raney Ni
Lee [50]	unknown	Ni foam	None or LDH-NiFe	Ni foam	None or Raney Ni
Loos [39]	unknown	unknown	Raney Ni	unknown	Raney Ni

Zirfon resistance we take this effect into account by increasing our calculated resistance with 5%.

2.2. Analysis of current–voltage curves

Current–voltage (IV) data from ten different sources were analyzed, all of them based on a zero gap configuration with a Zirfon diaphragm. The electrode materials of these sources are listed in Table 2.

The first step carried out in the analysis of the IV-data was the calculation of the reversible cell potential from the experimental conditions (temperature, pressure and KOH/NaOH concentration), for which Eqs. (4) and (5) as given by LeRoy were employed [19]. The reversible potential ($E_{rev,T,p}$) can be calculated from the absolute pressure p (in bar), the aqueous vapor pressure of the electrolyte solution p_{H_2O} (in bar), the vapor pressure of pure water $p_{H_2O}^0$ (in bar) and the reversible potential for standard pressures $E_{rev,T}^0$. The latter can be calculated using Eq. (5), where the temperature is in Kelvin. The vapor pressure above the KOH or NaOH electrolyte was obtained from the literature [13, 33].

$$E_{rev,T,p} = E_{rev,T}^0 + \frac{RT}{2F} \ln \left(\frac{P - P_{H_2O}}{P_{H_2O}/p_{H_2O}^0} \right)^{1.5} \quad (4)$$

$$E_{rev,T}^0 = 1.5184 - 1.5421 \cdot 10^{-3}T + 9.523 \cdot 10^{-5}T \ln T + 9.84 \cdot 10^{-8}T^2 \quad (5)$$

As a next step the IV-data were fitted to Eq. (6), in which E_{cell} is the measured cell potential in Volt, b is the Tafel slope in V/I the current density in A/cm^2 , I_0 the exchange current density in A/cm^2 and R the area resistance of the cell in Ωcm^2 . The fitting was carried by varying b , I_0 and R to minimize the standard error of regression in the fitted potential compared to the experimental value. It should be remarked that Eq. (6) can be derived from Eq. (7), which separately takes into account the anodic Tafel slope a , the cathodic Tafel slope c , the anodic exchange current density $I_{0,a}$ and the cathodic exchange current density $I_{0,c}$. Yet, the use of Eq. (7) is not practical, since it has too many fitting parameters. Eq. (7) converts to Eq. (6) if we define $b = a+c$ and $I_0 = I_{0,a}^{a/b} I_{0,c}^{c/b}$. Thus, b is the sum of the cathodic and anodic Tafel slopes and I_0 is a nonlinear average of the anodic and cathodic exchange current densities (I_0 lies in between $I_{0,a}$ and $I_{0,c}$).

$$E_{cell} = E_{rev,T,p} + b \log_{10} \frac{I}{I_0} + IR \quad (6)$$

$$E_{cell} = E_{rev,T,p} + a \log_{10} \frac{I}{I_{0,a}} + c \log_{10} \frac{I}{I_{0,c}} + IR \quad (7)$$

To be able to compare area resistance values of experiments at different temperatures and KOH concentrations we normalized to values at 30% KOH and 80 °C by applying Eq. (8), in which $R_{30\%KOH,80C}$

is the normalized area resistance and $\kappa_{30\%KOH,80C}$ is the conductivity of a 30% KOH electrolyte at 80 °C.

$$R_{30\%KOH,80C} = R \times \frac{\kappa}{\kappa_{30\%KOH,80C}} \quad (8)$$

2.3. Numerical simulation of the secondary current distribution in a zero gap configuration

Simulations of the secondary current distribution in a zero gap configuration were performed to explore the effect of the geometry of a representative electrode and the fluid volume fraction distribution in the cell upon the resistance.

The configuration used in the simulations is an axisymmetric model of a half-cell with a perforated plate electrode and a half-diaphragm, as shown in Fig. 1. If the pattern of holes in a perforated plate is hexagonal, the perforated plate can be regarded as a collection of “rings” with a circular inner boundary and a hexagonal outer boundary. The model contains one of these “rings”. The hexagonal outer boundary of the ring is replaced by a circular outer boundary, which is a reasonable approximation and makes the geometry axisymmetric [34]. The axial and radial coordinates of the axisymmetric domain are denoted by x and r , respectively. The axis $r=0$ is the axis of the hole in the ring. The ring electrode, denoted by the shaded area in Fig. 1, is an activated electrode: the nickel base is coated with a layer of Raney nickel (RaNi). The dimensions of the perforated plate and its coating correspond to the specifications provided by Kraglund et al. [22], who used a perforated plate for the anode and a nickel foam mesh for the cathode. The radius of the hole in the plate and the radius of the computational domain are 600 and 775 μm , respectively. Thus, the fraction of the open area of the electrode is $600^2/775^2 = 0.60$. The thickness of the Ni plate is 340 μm and the thickness of the coating 100 μm . The coating occurs only one side of the electrode, according to Fig. S6d in [22]. Coated perforated plates for both the anode and cathode were used by Schalenbach et al. [23] (hole radius 800 μm and open area fraction 0.66).

Aoki and Nishiki [35] employed a similar axisymmetric geometry for simulations of the effect of the inner and outer radii of the ring upon the resistance. One difference between our work and [35] is that we compute the secondary potential distribution instead of the primary distribution, which means that we include the spatially varying overpotential that drives the reaction at the electrode. Other differences are that our model mimics an activated electrode as used in recent experiments, that we investigate the effect of bubbles in the electrolyte, and that we use a finite volume method instead of a finite element method.

The potential $\phi(x,r)$ is solved in the computational domain Z , which consists of three zones: Z_0 (the half-diaphragm), Z_1 (the narrow gap between the electrode and the diaphragm), and Z_2 (the bulk region). The interior of the electrode, represented by the shaded regions, does not belong to the computational domain. In a

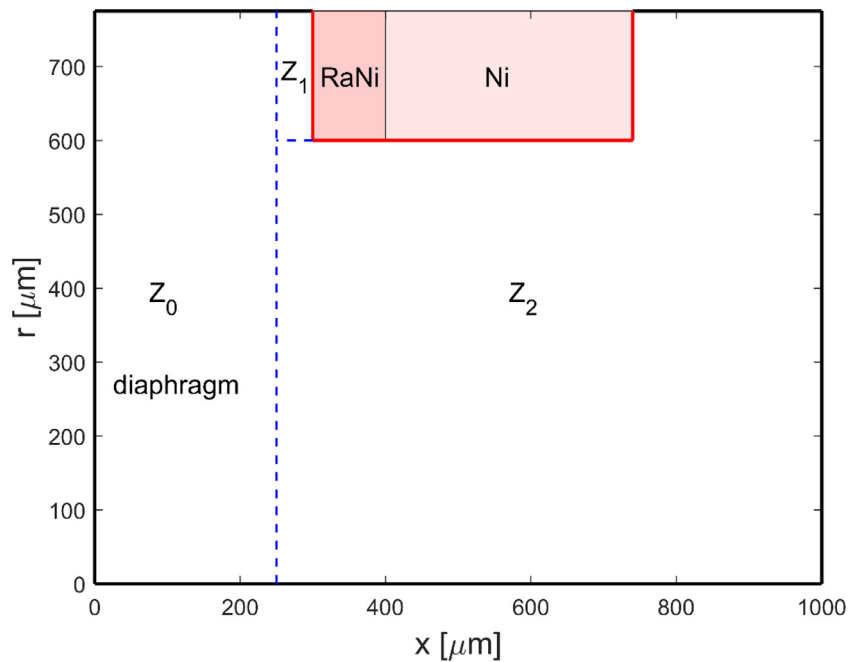


Fig. 1. Sketch of the axisymmetric computational domain corresponding to the right half-cell. The potential ϕ is solved in the white regions, zones Z_0 , Z_1 and Z_2 . Zone Z_0 represents the right half of the diaphragm, zone Z_1 the gap and zone Z_2 the bulk. The filled space denotes the perforated Ni plate electrode coated with RaNi. (For interpretation of the references to color in this figure, the reader is referred to the web version of this article.)

zero gap configuration, the electrode is pressed on the diaphragm, but this does not mean that the gap size is precisely zero. In fact, Kienzlen et al. [36] recommended a minimum hole diameter and a gap size of $200 \mu\text{m}$ to ensure mobility of the bubbles in the hole and the gap. Since we expect that the average gap size in recent experiments in which perforated plate electrodes were pressed on the diaphragm was considerably smaller than $200 \mu\text{m}$, we choose a gap size (axial length of zone Z_1) of $50 \mu\text{m}$ in our simulations, unless mentioned otherwise.

We introduce the local volume fractions $\alpha(x,r)$, $\beta(x,r)$ and $\gamma(x,r)$, where α is the volume fraction of the gas phase, β the volume fraction of the liquid phase and γ the volume fraction of the solid phase ($\alpha + \beta + \gamma = 1$). We approximate α , β and γ by piecewise constant functions: $\alpha = \alpha_i$, $\beta = \beta_i$ and $\gamma = \gamma_i$ in zone Z_i . The local effective conductivity $\lambda(x,r)$ is equal to λ_i in each zone Z_i , while each λ_i follows from the Bruggeman equation, $\lambda_i = \beta_i^{3/2} \kappa$.

The equation governing the electric potential ϕ in the computational domain Ω is given by:

$$\frac{\partial}{\partial x} \left(\lambda \frac{\partial \phi}{\partial x} \right) + \frac{1}{r} \frac{\partial}{\partial r} \left(\lambda r \frac{\partial \phi}{\partial r} \right) = 0. \quad (9)$$

At the left boundary, the midplane of the diaphragm ($x = 0$), $\phi = \phi_m$ is imposed, where ϕ_m is a prescribed constant. This means that the potential in the midplane is assumed to be spatially uniform. We will explain below that this is consistent with the assumption of a symmetric cell and equal absolute values of the overpotentials in the left and right half-cells.

At the bottom, top and right boundary (respectively $r = 0$, $r = r_{\text{max}} = 775 \mu\text{m}$ and $x = 1000 \mu\text{m}$ in Fig. 1), the boundary condition is $\partial \phi / \partial n = 0$, where n denotes that the derivative is taken along the vector normal to the boundary pointing outside the computational domain.

At the electrode surface the (thick red line pieces in Fig. 1) the boundary condition is given by the following Butler-Volmer equation,

$$j_e = \lambda \frac{\partial \phi}{\partial n} = j_0 (e^{f(\phi - \phi_0)} - e^{-f(\phi - \phi_0)}), \quad (10)$$

in which both the potential $\partial \phi / \partial n$ and potential ϕ vary along the electrode surface. Furthermore, j_e is the local current density at the electrode, j_0 is the local exchange current density, while ϕ_0 is a constant, equal to the potential of the electrode metal minus the equilibrium potential of the reaction at the electrode. Since we do not resolve the double layer, the numerical value of ϕ at the electrode represents the potential very close to the electrode but outside the double layer. Therefore, at the electrode $\phi - \phi_0$ is equal to the local overpotential, which drives the electrochemical reaction and is denoted by η . Since Eq. (9) expresses that the net current through the boundaries of a closed region is zero, the integral of j_e over the electrode is automatically the same as the integral of j_m over the midplane of the diaphragm, where j_m is the local current density at the midplane of the diaphragm, that is $\lambda \partial \phi / \partial x$ evaluated at $x=0$.

The exponential factor f in Eq. (10) is related to the Tafel slope by $f = 2 \ln(10)/b$. The factor 2 in the definition of f accounts for the attribution of half of the logarithmic slope b in Eq. (6) to the simulated half-cell. At the non-activated (Ni) part of the surface, $b = 0.155 \text{ V}$ and $j_0 = 0.33 \cdot 10^{-5} \text{ A/cm}^2$, while at the activated (RaNi) part of the electrode surface, $b = 0.082 \text{ V}$ and $j_0 = 3.65 \cdot 10^{-5} \text{ A/cm}^2$. These values correspond to the results from the fits of the experiments of Kraglund et al. [22] with non-activated and activated electrodes (see Table 3; the non-activated I_0 has been multiplied by $775^2 / (2 \cdot 600 \cdot 340 + 2 \cdot (775^2 - 600^2)) = 0.68$, the diaphragm surface area divided by the surface area of a non-coated perforated plate, and the activated I_0 has been multiplied by $775^2 / (2 \cdot 600 \cdot 100 + (775^2 - 600^2)) = 1.67$, the diaphragm surface area divided by the surface area of the RaNi coating of a one-sided coated perforated plate).

Thus, we assume that the kinetic parameters, a and j_0 , and the corresponding overpotentials are the same in both half cells. This assumption implies that if we extend the half-cell geometry to a full cell geometry by mirroring the geometry in Fig. 1 with respect to $x = 0$ (the midplane of the diaphragm) then, up to a constant, the potential distribution at the right side is a mirrored version of the potential distribution at the left side. It particularly implies

that the potential at the midplane of the diaphragm is constant if the full domain is simulated (this was verified). Since we are only interested in potential differences, the choice for ϕ_m can be arbitrary, and we choose $\phi_m = 0$ V. The constant potential ϕ_0 in Eq. (9) is determined by the constraint that the current density radially averaged over the midplane of the diaphragm ($x=0$) is equal to 1 A/m² (the absolute value of this averaged value corresponds to the current density I previously defined). This implies that $\phi_0 - \phi_m > 0$. The positive sign indicates that the simulated half-cell is the anodic one.

In the following, we introduce the procedure for the computation of the ohmic area resistance R of the cell from integral over the volume local heat generation ($\lambda|\nabla\phi|^2$, expressed in W/m³):

$$R = \frac{2 \int_Z \lambda |\nabla\phi|^2 dZ}{I^2 A_d} \quad (11)$$

where $A_d = \pi r_{\max}^2$ is the area of the (surface) of the diaphragm, $Z = Z_0 \cup Z_1 \cup Z_2$ is the computational domain. The factor 2 follows from our symmetry assumption and the fact that Z is only the volume of the half-cell. Furthermore, we remind that R is the area resistance and I the nominal current density (IA_d is the current). For the local heat generation, we can write

$$\begin{aligned} \lambda|\nabla\phi|^2 &= \nabla \cdot (\lambda\phi\nabla\phi) - \phi\nabla \cdot (\lambda\nabla\phi) \\ &= \nabla \cdot (\lambda\phi\nabla\phi) = -\nabla \cdot (\mathbf{j}\phi). \end{aligned} \quad (12)$$

To derive the second equality, we used Eq. (8), which can be written as $\nabla \cdot (\lambda\nabla\phi) = 0$, and for the third equality we defined the current density vector $\mathbf{j} = -\lambda\nabla\phi$. Next, we substitute Eq. (12) into Eq. (11):

$$\begin{aligned} R &= \frac{-2 \int_Z \nabla \cdot (\mathbf{j}\phi) dZ}{I^2 A_d} = \frac{-2 \int_{S_e} \phi \mathbf{j} \cdot \mathbf{n} dS_e - 2 \int_{S_m} \phi \mathbf{j} \cdot \mathbf{n} dS_m}{I^2 A_d} \\ &= \frac{2(\phi_e - \phi_m)}{I}. \end{aligned} \quad (13)$$

In Eq. (13), the divergence theorem of Gauss is used to transform the volume integral over Z to integrals over the electrode surface S_e and the midplane of the diaphragm S_m , while \mathbf{n} is the outward-pointing local normal vector. Furthermore, ϕ_e is the average of ϕ at the electrode weighted by the current density:

$$\phi_e = \frac{\int_{S_e} \mathbf{j}_e \phi dS_e}{\int_{S_e} \mathbf{j}_e dS_e} = \frac{\int_{S_e} \mathbf{j}_e \phi dS_e}{IA_d}. \quad (14)$$

Since ϕ at the midplane of the diaphragm is constant (by definition), the weighted average of ϕ at this plane is simply equal to the previously defined constant ϕ_m . In our simulations, we use ϕ_e to compute R , but also to obtain the current density weighted average of the overpotential, $\eta_e = \phi_0 - \phi_e$.

In the same way, we define the resistance over only the diaphragm by

$$R_d = \frac{2 \int_{Z_0} \lambda |\nabla\phi|^2 dZ_0}{I^2 A_d} = \frac{2(\phi_d - \phi_m)}{I} \quad (15)$$

where ϕ_d is the average of ϕ at the surface of the diaphragm S_d ($x=250$ μ m) weighted by the current density $j_d = \lambda \partial\phi/\partial x$ at this surface,

$$\phi_d = \frac{\int_{S_d} \mathbf{j}_d \phi dS_d}{\int_{S_d} \mathbf{j}_d dS_d} = \frac{\int_{S_d} \mathbf{j}_d \phi dS_d}{IA_d}. \quad (16)$$

The numerical method used in the simulations was implemented in Fortran. The potential equation is discretized by a finite volume method. The potential is stored at the centers of the Cartesian grid. Second-order central differences are used for the derivatives. To treat the nonlinear mixed boundary equation given in Eq. (10), the Newton-Raphson method is incorporated in the general iterative

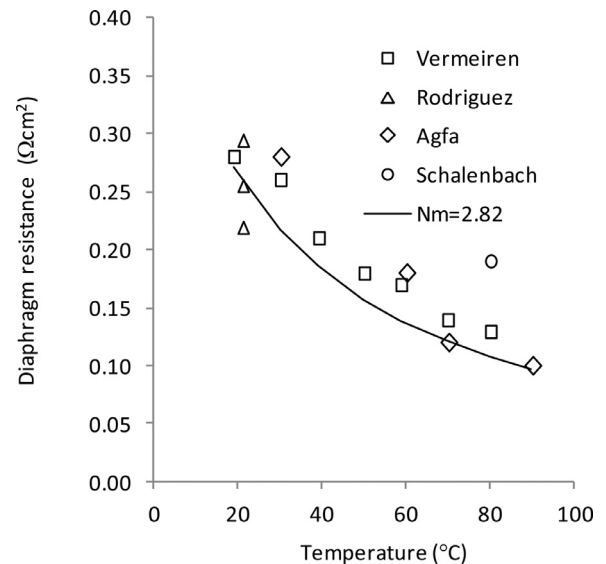


Fig. 2. Comparison of estimated Zirfon resistance using $N_m=2.82$ (–) to available experimental data of Vermeiren [9], Rodriguez [37], Schalenbach [21] and Agfa [28, 49] in 30% KOH. The number for Schalenbach of $0.19 \Omega \text{ cm}^2$ is based on a conductivity of 0.241 S cm^{-1} as measured with ex-situ impedance spectroscopy and a diaphragm thickness of 0.46 mm . Estimated resistance is based on a porosity of 50% and a diaphragm thickness of 0.5 mm . An addition of 5% is made to the calculated resistance values to compensate for the effect of the open mesh support structure.

procedure. A proportional integral control algorithm is used to determine ϕ_0 such that the radially averaged value of j_m converges to the desired value.

The base grid consists of 105×80 cells, 105 cells in the axial and 80 cells in the radial direction (including the 45×20 inactive cells in the interior of the electrode). The grid size is approximately $10 \mu\text{m}$ in both directions, except that the axial grid size between $250 \leq x \leq 300 \mu\text{m}$ is approximately $5 \mu\text{m}$, so that the gap size is represented by 10 grid cells. This grid was verified to be sufficiently fine by repeating two representative simulations on a grid refined by a factor two in each direction and observing that R and R_d changed by less than 1%.

3. Results and discussion

3.1. Analysis of diaphragm conductivity

Fig. 2 shows reported experimental data on Zirfon resistance [9, 28, 37] at different temperatures. The figure shows that there is a relatively large spread in the experimental data, which suggests that it is relatively difficult to accurately determine the diaphragm resistance. This is confirmed by the data of Rodriguez et al. that show a significant difference in resistance values for different measurement methods [37]. Nevertheless, except for the resistance reported by Schalenbach [21], the points data from the literature show a consistent decrease of the diaphragm resistance with increasing temperature.

The figure also shows the Zirfon resistance estimated based on the electrolyte conductivity and a MacMullin number of 2.8. This MacMullin number is valid for a porous medium consisting of spheres and a diaphragm porosity of 50%. Comparing the estimated diaphragm resistance to the experimental data one can conclude that there is a good agreement in the temperature dependence of the resistance. This confirms that the Zirfon resistance is indeed directly related to the resistance of the KOH electrolyte that fills its pores. One can also see that most experimental points are above the estimated line, which suggests that the MacMullin number of Zirfon is actually above 2.8. In turn, this suggests that describing

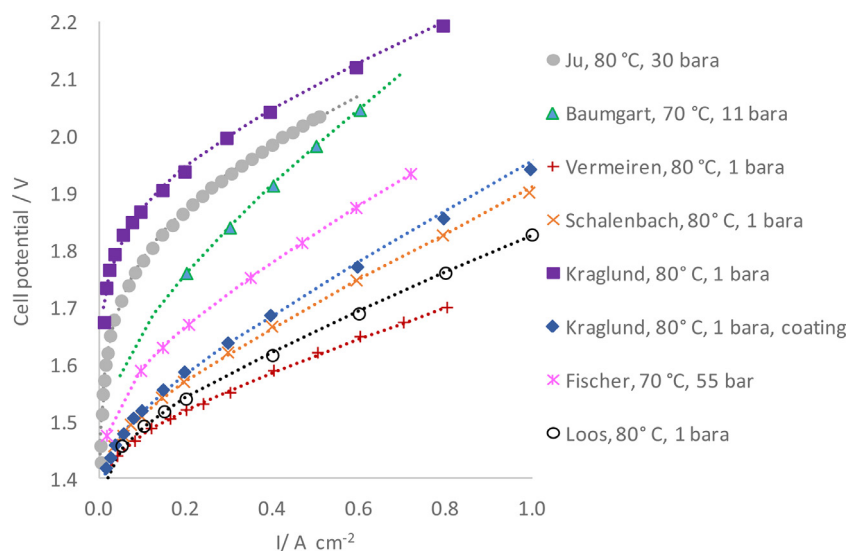


Fig. 3. Selected IV-curves of zero gap alkaline electrolyzers employing Zirfon as separator. Relevant experimental conditions are listed in Table 3. The dotted lines indicate the fits made. For the Kraglund data, the word coating means that a catalytic coating is applied on the cathode.

the Zirfon diaphragm as a porous medium consisting of spheres is inaccurate. Based on the experimental data one can roughly estimate the MacMullin number to be around 3.2, which is in the middle of the range of 2.5 to 4.0 as suggested by other correlations for the MacMullin number [27, 30]. Due to the large spread in the experimental data and the large standard deviation of the porosity of 20%, it is not possible to say which MacMullin correlation is most accurate. This would require more research into the tortuosity factor of the Zirfon diaphragm. Nevertheless, from our analysis we can draw the general conclusion that the resistance of the Zirfon diaphragm seems to be as expected for a porous separator.

3.2. Analysis of IV-curves

Zero gap alkaline electrolyzers with Zirfon as a separator have been investigated in a number of papers [17, 20, 38, 39] and Fig. 3 shows selected current–voltage relations from these works. All depicted curves were recorded in strong KOH electrolyte (24–30 wt%) at a temperature of 70–80 °C. An overview of the electrode materials can be found in Table 2 and the experimental conditions are listed in Table 3.

The figure shows that certain current–voltage curves are at much higher potentials than others. These differences can be primarily ascribed to the use of electrodes with active coatings, which have a much lower overpotential than unactivated nickel electrodes as mostly clearly shown by the two curves from the work of Kraglund. Yet, there are also more subtle differences such as the difference in slope between the works of Schalenbach and Vermeiren, both of which making use of activated electrodes. The lower slope is an indication that the area resistance in the work of Vermeiren is significantly lower than in the work of Schalenbach, even though they are both zero gap configurations using comparable electrode coatings.

To further elucidate the contribution of the area resistance to the cell potential, the curves were fitted according to Eq. (6), in which the Tafel slope, exchange current density and area resistance were used as fitting parameters. The results of this fitting are given in Table 3 and shown in Figure 3. We realize this type of fitting is not perfect, since it fails to take into account current density dependent cell potential contributors such as the effect of bubbles or mass transfer limitations. Yet, the fits match the experimental

lines well, which would not be possible if there would be a cell potential contributor with a more than linear increase with current density.

In order to be able to compare the area resistances of the different experiments we need to take into account the differences in temperature and KOH concentration. We have normalized all area resistances to 30 wt% KOH and 80 °C by multiplying the measured area resistance with the electrolyte conductivity of the experiment and dividing by the electrolyte conductivity of a 30% KOH solution of 80 °C (1.38 S/cm) as shown in Eq. (8). Since Zirfon is a porous diaphragm, its conductivity should be directly proportional to the electrolyte conductivity. The results are given in Table 3 and graphically depicted in Fig. 4, where the area resistances of the different experiments are plotted from low to high values. Fig. 4 also shows the expected diaphragm resistance as depicted in Fig. 2.

The main conclusion that can be drawn from Fig. 4 is that all area resistances are much higher than the expected diaphragm resistance of $0.13 \Omega \text{ cm}^2$. Most measured values are in the range of 0.24 to $0.4 \Omega \text{ cm}^2$. There are even some values above $0.4 \Omega \text{ cm}^2$, for which we expect that there are additional area resistances in the cell/stack, e.g. related to poor electrical contacts. Closest value to the diaphragm resistance is the value deduced for the work of Vermeiren ($0.24 \Omega \text{ cm}^2$), but even that value is almost a factor two higher than the expected diaphragm resistance. The results therefore suggest that there must be a large additional ohmic contributor in these zero gap cells next to the diaphragm resistance.

It is interesting to note that there does not seem to be a strong dependence on pressure, which one might expect if bubbles would play a role. This can be concluded from the fact that the results of Ju and Fischer are comparable to the other results and that the Fischer results do not show significant pressure dependence. Similarly there is no apparent influence of electrode activation with bare nickel electrodes giving comparable results to activated electrodes. The work of Phillips suggests that there might be a temperature dependence (after normalization), but this is not seen in the data from Ju and Fischer.

A number of zero gap configurations have also been investigated with impedance spectroscopy. Impedance spectroscopy has the advantage that it allows for a clear discrimination between area resistances and electrode overpotentials and is hence a better method than deducing the area resistance from the current–voltage curve. Unfortunately, impedance spectroscopy has only

Table 3

Fitted values of current–voltage curves of experiments with a zero gap cell employing Zirfon as separator of 0.5 mm.

Ref.	T (°C)	P (bar)	C (wt%)	E_c (V)	I_0 (A/cm ²) ^a 10^{-5}	η (V) @ 0.2 A/cm ²	b (V)	R (Ω cm ²)	κ (S/cm)	$R_{30\% \text{ KOH}, 80^\circ\text{C}}$ (Ω cm ²)
Vermeiren [9]	80	1	29%	1.182	0.32	0.29	0.060	0.24	1.37	0.24
Vermeiren [9]	90	1	29%	1.169	1.1	0.28	0.066	0.22	1.52	0.24
Ju [20]	80	30	30%	1.268	42	0.56	0.207	0.25	1.38	0.25
Ju [20]	60	30	30%	1.280	15	0.58	0.184	0.35	1.09	0.28
Ju [20]	30	30	30%	1.298	0.95	0.65	0.150	0.55	0.68	0.27
Schalenbach [21]	80	1	30%	1.183	0.39	0.32	0.067	0.37	1.38	0.37
Baumgart [24]	67	5	30%	1.236	0.43	0.31	0.067	0.73	1.19	0.63
Baumgart [24]	70	18	30%	1.263	0.17	0.35	0.068	0.63	1.23	0.56
Baumgart [24]	70	11	30%	1.252	76	0.38	0.167	0.52	1.23	0.46
Bowen [25]	70	5	30% ^b	1.234	0.053	0.70	0.125	0.86	1.23	0.76
Bowen [25]	70	5	30% ^b	1.234	93	0.19	0.055	0.88	1.23	0.78
Phillips [17]	30	1	1M ^a	1.225	0.45	0.89	0.191	1.71	0.204	0.25
Phillips [17]	40	1	1M ^a	1.216	0.19	0.84	0.167	1.70	0.238	0.29
Phillips [17]	50	1	1M ^a	1.207	0.16	0.79	0.156	1.69	0.272	0.33
Phillips [17]	60	1	1M ^a	1.197	0.25	0.78	0.159	1.60	0.306	0.36
Phillips [17]	70	1	1M ^a	1.184	0.21	0.75	0.151	1.58	0.340	0.39
Phillips [17]	80	1	1M ^a	1.171	0.21	0.73	0.147	1.54	0.374	0.42
Kraglund [22] (coating) ^c	80	1	24%	1.178	2.2	0.33	0.082	0.39	1.28	0.36
Kraglund [22] (no coating)	80	1	24%	1.178	0.49	0.70	0.155	0.27	1.28	0.25
Kraglund [23]	80	1	24%	1.178	0.13	0.71	0.138	0.30	1.28	0.28
Fischer [38]	50	55	28%	1.298	11	0.32	0.098	0.52	0.94	0.35
Fischer [38]	60	55	28%	1.292	21	0.32	0.106	0.44	1.07	0.34
Fischer [38]	70	10	28%	1.248	27	0.32	0.113	0.41	1.21	0.36
Fischer [38]	70	20	28%	1.264	37	0.31	0.114	0.41	1.21	0.36
Fischer [38]	70	30	28%	1.273	30	0.30	0.107	0.40	1.21	0.35
Fischer [38]	70	40	28%	1.280	48	0.31	0.118	0.38	1.21	0.34
Fischer [38]	70	50	28%	1.284	35	0.30	0.110	0.40	1.21	0.35
Fischer [38]	70	55	28%	1.287	36	0.30	0.109	0.40	1.21	0.35
Lee (no coating) [50]	80	1	30%	1.183	0.28	0.55	0.11	0.492	1.38	0.49
Lee (coating) [50]	80	1	30%	1.183	0.088	0.35	0.07	0.42	1.38	0.42
Loos [39]	80	1	30%	1.183	3.7	0.30	0.081	0.28	1.38	0.28

^a NaOH.^b Assumption, actual concentration unknown.^c a catalytic coating is applied on the cathode.

been carried out for few of the listed zero gap electrolyzers [17, 21–23]. The measured high frequency resistances are listed in the Supporting Information. In general the impedance resistances are significantly lower than the fitted area resistances (although this is not the case in the work of Kraglund [23]). At the moment we do not have a clear explanation for this and this is an area for future investigation. We also observe that impedance values seem to be higher at high current densities than at low current densities. This might be due to possible effect of bubbles, but we have too little data to confirm this.

Even though the resistances measured with impedance spectroscopy are lower than the fitted area resistance they are still significantly higher than the diaphragm resistance. Therefore, we can still conclude that the measured resistance cannot be explained from the diaphragm resistance alone. The closest value is deduced to be $0.17 \Omega \text{ cm}^2$ from the impedance experiment at 30°C of Phillips, but it should be remarked that for this experiment the normalization has a large effect, since the experiment has been carried out in 1M NaOH at 30°C , where the conductivity of the electrolyte is much lower. Therefore, interpretation of this result should be carried out with care.

To find out whether the increased area resistance observed in the zero gap configuration is something unique to Zirfon we also looked at zero gap electrolyzers with other diaphragm materials. Results with asbestos [40], nickel oxide [41,42], polysulfone [43] and an ultrafiltration membrane (Supor-200) [44] are shown in the Supporting Information. For the configuration with the ultrafiltration membrane a low resistance of $0.114 \Omega \text{ cm}^2$ was determined. Yet, this membrane only had a thickness of 0.14 mm, which means that a diaphragm resistance in the order of $0.03 \Omega \text{ cm}^2$ would be expected (assuming a porosity and tortuosity factor com-

parable to Zirfon). This means that also for this diaphragm the expected resistance is higher than expected. For the other diaphragms the fitted area resistances are significantly higher ($0.3\text{--}1.0 \Omega \text{ cm}^2$). Although the thickness is not known for all of these materials, these values are so high that it is unlikely that they equal the pure diaphragm resistance. Therefore, we can conclude that the increased area resistance is probably not uniquely related to Zirfon.

3.3. Estimation of the resistance in a zero gap configuration

To estimate the effect of the zero gap geometry and the gas phase on the area resistance, we simulate the potential distribution and the resulting area resistance for the cases defined in Table 4. The definition of variables, the governing equations and the method can be found in the methods section. All simulations are performed for a nominal current density $I = 1 \text{ A/cm}^2$, an electrolyte conductivity $\kappa = 1.38 \Omega^{-1} \text{ cm}^{-1}$ (value for 80°C), and a diaphragm porosity of 0.484 ($\epsilon = \beta_0 = 0.484$), so that the effective conductivity in the diaphragm $\lambda_0 = \beta_0^{3/2} \kappa = 0.465 \Omega^{-1} \text{ cm}^{-1}$ is equal to $0.5^{1.5} \kappa / 1.05$. In other words, the diaphragm conductivity corresponds to a porosity of 0.5 and a correction by a factor $1/1.05$ for the effect of the mesh-fabric support structure. This implies that the reference diaphragm resistance is $R_{d,0} = 0.05 \text{ cm} / (0.465 \Omega^{-1} \text{ cm}^{-1}) = 0.108 \Omega \text{ cm}^2$.

The differences among the cases are due to variations in α_1 and α_2 , the gas volume fractions in the gap (zone Z_1) and bulk (zone Z_2). For these fractions, we use the values 0 (no gas-phase), 0.3 (a moderately dense dispersion of bubbles in the electrolyte) and 0.6 (a very dense dispersion of bubbles in electrolyte). Furthermore, $\alpha_1 = 0.999 \approx 1$ represents an insulating gas layer that fills the entire

Table 4

Definition and results of simulation cases A0–8 in series A. In this series the gap size is 50 μm and $I = 1.0 \text{ A/cm}^2$. The gas volume fractions in zones 1 and 2 (α_1 and α_2) are input parameters.

Case	α_1 (gap)	α_2 (bulk)	ϕ_0 [V]	ϕ_e [V]	η_e [V]	R_d [$\Omega \text{ cm}^2$]	R [$\Omega \text{ cm}^2$]
A0	0	0	0.269	0.065	0.204	0.110	0.131
A1	0.3	0	0.271	0.067	0.204	0.110	0.135
A2	0.6	0	0.276	0.072	0.204	0.109	0.145
A3	0.999	0	0.320	0.097	0.223	0.134	0.194
A4	0.3	0.3	0.276	0.072	0.203	0.113	0.145
A5	0.6	0.3	0.282	0.079	0.204	0.112	0.157
A6	0.999	0.3	0.341	0.118	0.223	0.135	0.236
A7	0.6	0.6	0.295	0.092	0.203	0.120	0.183
A8	0.999	0.6	0.404	0.181	0.224	0.139	0.361

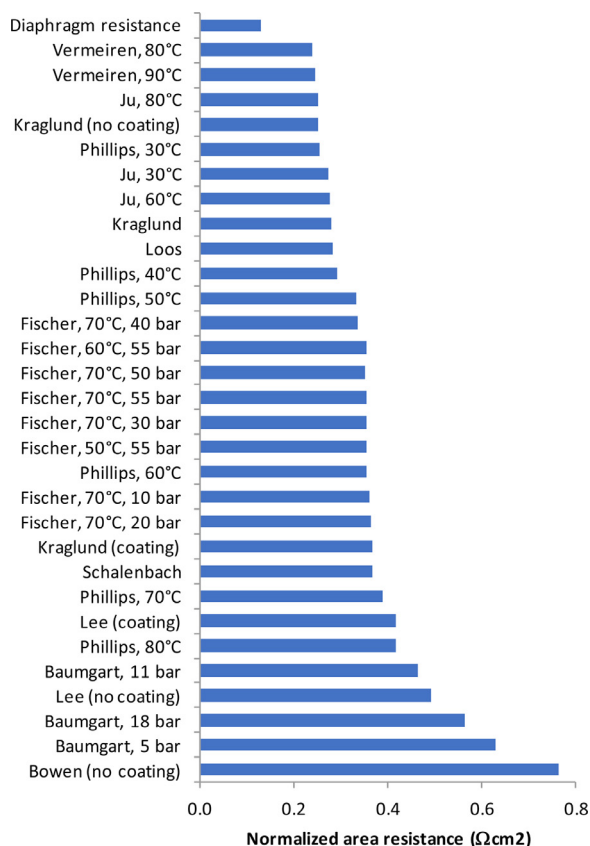


Fig. 4. Comparison of normalized area resistance for different zero gap alkaline electrolyzers (blue bars). All area resistances are normalized to 30 wt% KOH and 80 °C. The depicted diaphragm resistance is 0.13 $\Omega \text{ cm}^2$ (based on work of Vermeiren). (For interpretation of the references to color in this figure legend, the reader is referred to the web version of this article.)

gap. A gas volume fraction of 0.6 is high for a bubbly flow, but not unrealistic; an overall gas volume fraction of approximately 0.6 has been measured in a lab-scale electrolyzer [44] and also in a bubble column reactor with a microbubble dispersion [45]. Furthermore, the experiments of Kienzlen et al. [36] support the existence of an insulating stagnant gas layer if the gap size is smaller than 200 μm . Such a gas layer can be stagnant, because the capillary force over an interface across a narrow gap can easily balance the buoyancy force exerted on the gas layer in the gap. In fact, when the gas fraction of bubbles in the gap becomes high (say 0.6), one of the following three scenarios might occur. In the first scenario, the gas fraction remains about 0.6, because the flow dynamics in the gap is such that bubbles keep being generated and removed, while the electrolyte keeps being refreshed. In the second scenario,

the high bubble volume fraction causes a strong suppression of the mixing and motion in the gas-liquid mixture. Thus, the gap is filled with a stagnant packed collection of bubbles. In this scenario, the mixing is reduced that much that mass transfer of the reactant becomes limiting and reduces the current density in the gap to zero. In the third scenario, an insufficient amount of bubbles can escape from the gap, but the gas production can continue above a volume fraction of 0.6. With increasing volume fraction the bubbles are deformed and coalesce until the gap is (nearly) entirely filled with a dry foam or just gas. In both the second and third scenario, the current density in the gap is negligible. Therefore, the cases with $\alpha_1 = 0.999$ serve to illustrate these two scenarios, while the first scenario is illustrated by the cases with $\alpha_1 = 0.6$.

Next, we discuss the values of the resistance R reported in Table 4. In the first case, case A0, no gas is included. Nonetheless, the resistance in this case ($R = 0.131 \Omega \text{ cm}^2$) is larger than the reference diaphragm resistance $R_{d,0} = 0.108 \Omega \text{ cm}^2$. The reason is that this specific zero gap geometry deviates from the ideal zero gap geometry, in which each electrode would be a non-perforated plate at zero distance from the diaphragm. Thus, this specific zero gap geometry leads to an increase of the resistance by about $0.023 \Omega \text{ cm}^2$. The next three cases (A1–3) show the effect of a nonzero gas fraction in the gap, while the gas fraction in the bulk remains negligible ($\alpha_2 = 0$). Then the resistance increases by $0.063 \Omega \text{ cm}^2$ at most ($R = 0.194 \Omega \text{ cm}^2$ in case A3). The next three cases, A4, A5 and A6 can be compared to cases A1, A2 and A3, respectively, with the difference that the gas fraction in the bulk in cases A4–6 is not zero but moderately high ($\alpha_2 = 0.3$). In this triple, the effect of an increase of the gas fraction in the gap from 0.3 (case A4) to 0.999 (case A6) is significantly larger than in the triple A1–3. The computed resistance in case A6, in which the gap acts as an insulation layer, is $0.236 \Omega \text{ cm}^2 \approx 2.2 R_{d,0}$. In the last case listed in the table (case A8), the gas fraction in the bulk is very high ($\alpha_2 = 0.6$), while the gap again acts as an insulation layer. In this rather extreme case, we find $R = 0.361 \Omega \text{ cm}^2 \approx 3.3 R_{d,0}$.

The local distribution of the potential is shown in Fig. 5, for cases A0, A4, A5 and A6. The zero-gap geometry leads to nontrivial shapes of the potential isolines, and this pattern is modified by the presence of gas. In case A0, the distance between adjacent isolines is relatively small in the part of the diaphragm opposite to the gap, indicating that in this region the current and the resistance are relatively large. A similar observation is made for cases A4 and A5. In contrast, case A6 shows an increased distance of adjacent isolines in this region of the diaphragm. The reason is that in this case, the gas in the gap acts as an insulation layer; the current across the gap is blocked by the gas. Furthermore, the negligible effective conductivity in the gap leads to an accumulation of isolines in the gap.

For the same four cases, profiles along the electrode and the diaphragm surface are shown in Fig. 6. In Fig. 6a–c, the profile of

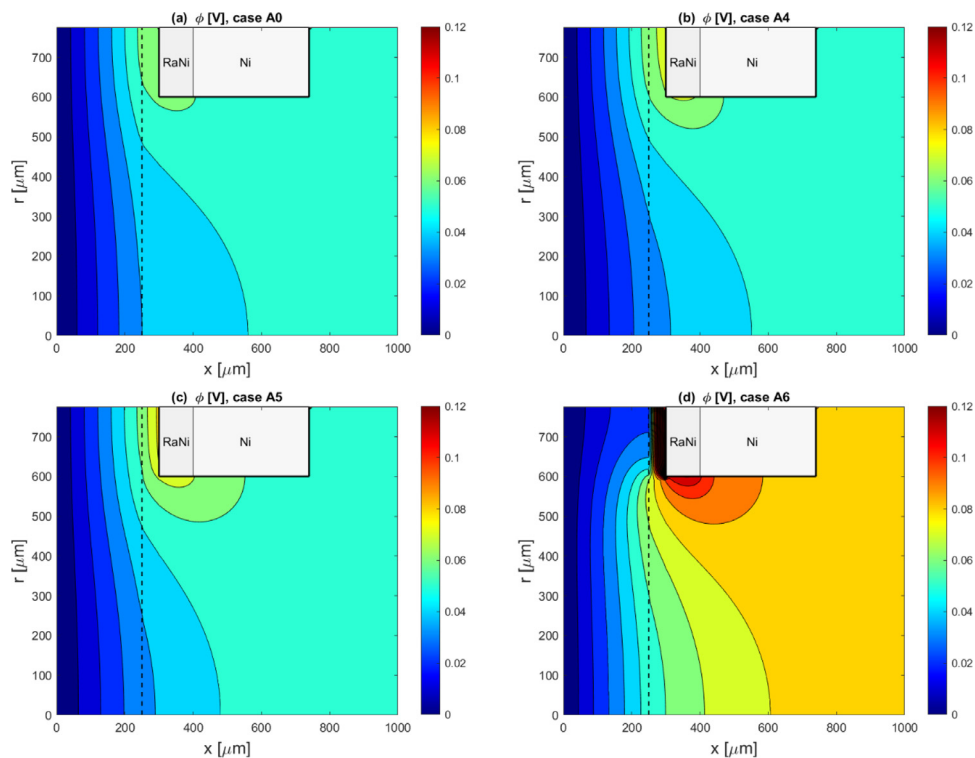


Fig. 5. Contours of the potential ϕ [V]. Results from simulations A0 (a), A4 (b), A5 (c) and A6 (d). The contour increment is 0.01 V. Values above the maximum of the color range (0.12) are also indicated by dark red. The dashed demarcation line at $x = 250 \mu\text{m}$ represents the diaphragm surface. (For interpretation of the references to color in this figure legend, the reader is referred to the web version of this article.)

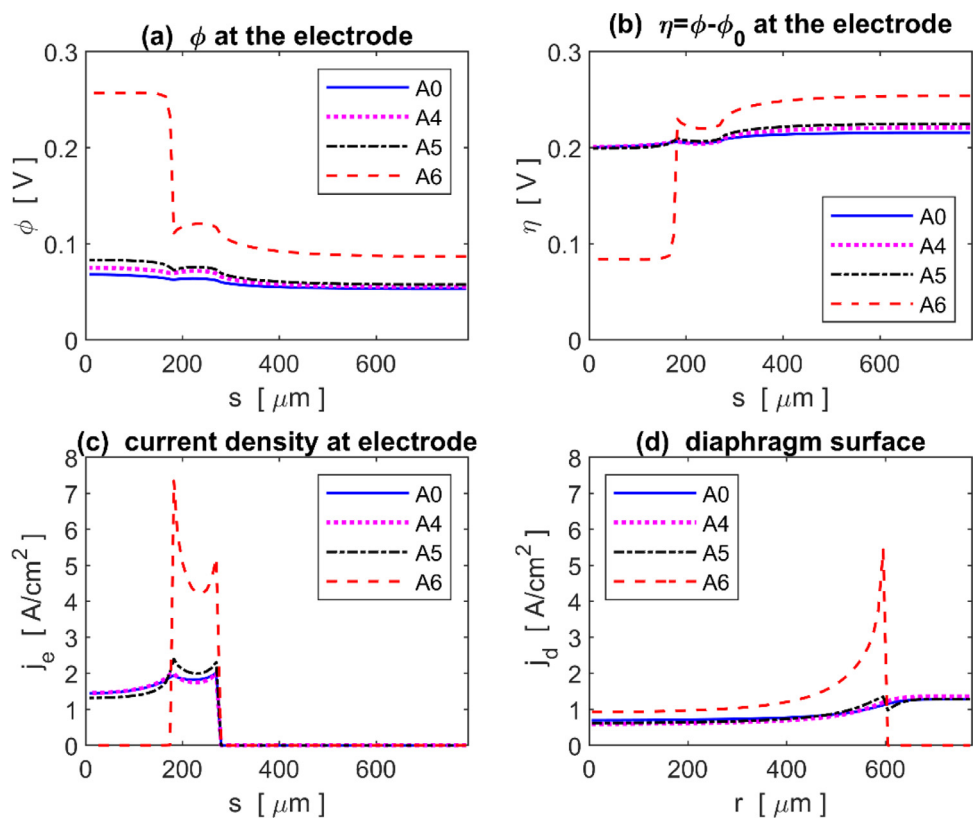


Fig. 6. The profiles of the potential ϕ at the electrode (a), the overpotential η (b), the current density at the electrode (c) and the current density through the diaphragm surface (d), for cases A0, A4, A5 and A6.

Table 5

The effect of a larger gap size on the average resistance and the effective resistance of the diaphragm for the various cases ($I = 1.0 \text{ A/cm}^2$ in all simulations)

Case	α_1 (gap)	α_2 (bulk)	Series B Gapsize 100 μm		Series C Gapsize 200 μm		Series D Gapsize 500 μm	
			R_d [$\Omega \text{ cm}^2$]	R [$\Omega \text{ cm}^2$]	R_d [$\Omega \text{ cm}^2$]	R [$\Omega \text{ cm}^2$]	R_d [$\Omega \text{ cm}^2$]	R [$\Omega \text{ cm}^2$]
0	0	0	0.109	0.137	0.107	0.150	0.107	0.193
1	0.3	0	0.108	0.144	0.107	0.162	0.107	0.216
2	0.6	0	0.108	0.159	0.108	0.186	0.110	0.253
3	0.999	0	0.134	0.209	0.134	0.235	0.134	0.310
4	0.3	0.3	0.111	0.156	0.108	0.214	0.107	0.254
5	0.6	0.3	0.109	0.171	0.108	0.110	0.109	0.315
6	0.999	0.3	0.135	0.261	0.135	0.306	0.136	0.433
7	0.6	0.6	0.116	0.214	0.111	0.273	0.108	0.446
8	0.999	0.6	0.138	0.421	0.138	0.526	0.139	0.818

ϕ at the electrode, the overpotential η and the current density j_e at the electrode are shown. These profiles are a function of s , the chord length along the electrode, which starts off at the core of the gap. More precisely, $s = 0, 175, 615$ and $790 \mu\text{m}$ correspond to the locations $(x,r) = (300, 775), (300, 600), (740, 600)$ and $(740, 775) \mu\text{m}$, respectively. Each curve clearly shows three parts: the Raney-nickel part in the gap ($0 \leq s \leq 175 \mu\text{m}$), the Raney-nickel part outside the gap ($175 \leq s \leq 275 \mu\text{m}$) and the nickel part of the electrode ($s \geq 275 \mu\text{m}$). In all cases, the current density is very small on the nickel part of the electrode. The increase from zero gas volume fraction (A0) to moderate gas volume fraction in the gap and the bulk (A4) has no significant effect on the shape of the profiles, although it does increase the level of ϕ . Fig. 6c clearly shows that a gas fraction of 0.999 in the gap in case A6 leads to negligible current density in the gap and thus also a negligible current density through the part of the diaphragm surface adjacent to the gap (Fig. 6d) Since the nominal current density is not changed, the current density on the Raney-nickel part outside the gap is strongly increased in this case. Because of the very low conductivity in the gap, the entire current density is maintained by a rather small part of the electrode ($175 \leq s \leq 275 \mu\text{m}$). As a result, the current density through and the resistance of the gas-liquid bulk mixture between this part of the electrode and the diaphragm are relatively large (see also the isolines in Fig. 5d). The relatively large current density through a rather small region in the bulk is the reason that R in case A8 is much larger than in case A6. In case A8, the gas fraction in the bulk is 0.6 compared to 0.3 in case A6, and the corresponding effective conductivities differ by a factor of nearly 3.

Although the current density on the diaphragm surface is not uniform (Fig. 6d), the computed diaphragm resistance R_d (Table 4) shows a negligible increase over the ideal value $R_{d,0} = 0.108 \Omega \text{ cm}^2$, unless the gap is full of gas ($\alpha_1 = 0.999$).

To illustrate the effect of a larger gap size than $50 \mu\text{m}$ (used in series A in Table 4), results for larger gap sizes are shown in Table 5. As expected, the total area resistance R increases with increasing gap size, and this effect is more pronounced if the gas fractions are nonzero. Comparison of the results of series B ($100 \mu\text{m}$ gap size) to those of series A, shows that doubling the small gap size in series A does not lead to large increases of R ; without bubbles the effect is 5% (compare case B0 to case A0) and with bubbles it is at most 17% (compare case B8 to case A8). To obtain much larger increases of R , the gap size has to be increased to a large value of e.g. $500 \mu\text{m}$ (series D in Table 5), which is unrealistically large for a well-designed zero gap configuration. For completeness, we mention that in some cases (e.g. C0 and D0) the computed diaphragm resistance R_d is $0.107 \Omega \text{ cm}^2$, which is slightly below the ideal diaphragm resistance $R_{d,0}$, while in reality the resistance cannot be lower than the ideal resistance. However, this discrepancy is small and within the 1% estimate for the numerical error (truncation error) in the computed resistances.

3.4. Discussion: possible causes of increased area resistance

The simulations can help us in identifying possible explanations for the increased resistances of zero gap electrolysis experiments compared to the expected diaphragm resistance. The simulations also allow us to quantify some of these effects.

- *Electrode geometry and uneven current distribution.* We simulated the potential distribution in a realistic zero gap configuration and found a resistance of approximately $0.13 \Omega \text{ cm}^2$ when the effect of gas was not included. This is about 20% or $0.02 \Omega \text{ cm}^2$ higher than the resistance of the diaphragm. This increase is a result of the uneven current distribution, which originates from the perforated plate electrode geometry.
- *An electrode gap.* Although in theory a zero gap configuration means that the electrodes are pushed against the diaphragm, in practice manufacturing techniques for large industrial electrolyzers are just not accurate enough to ensure that the gap is truly zero along the complete surface area of the diaphragm on both the cathode and the anode side. For this reason, we used a nonzero gap size in our simulations. The default value of the gap size was small ($50 \mu\text{m}$). Due to the high conductivity of the KOH electrolyte, the effect of this gap on the resistance is limited. From additional simulations with larger gap sizes, we conclude that the gap size needs to be quite large to influence the resistance at least if no gas volume is included (the resistance increased from $0.131 \Omega \text{ cm}^2$ to $0.137 \Omega \text{ cm}^2$ or $0.193 \Omega \text{ cm}^2$ when the gap size was increased from $50 \mu\text{m}$ to $100 \mu\text{m}$ or $500 \mu\text{m}$, respectively). Thus, a gap of $500 \mu\text{m}$ can potentially contribute $0.06 \Omega \text{ cm}^2$, yet this is not a realistic gap size in a well-designed zero gap electrolyzer.
- *Bubbles in the electrolyte.* We performed simulations for various values of the gas volume fractions in the narrow gap (α_1) and in the bulk (α_2). For a moderately dense flow ($\alpha_1 = \alpha_2 = 0.3$), we found a resistance of $0.145 \Omega \text{ cm}^2$, which is only $0.014 \Omega \text{ cm}^2$ higher than for the case without bubbles. Yet, the gas hold-up in alkaline electrolyzers can be large, over 50% at high current densities [46] and the narrow gap can even be entirely filled with gas [36]. For a gap entirely filled with gas, we found a resistance of $0.194 \Omega \text{ cm}^2$ when the gas fraction in the bulk was assumed to be zero and considerably higher resistances (up to $0.361 \Omega \text{ cm}^2$) when the gas fraction in the bulk was nonzero. Yet, if bubbles in the bulk play a key role, it is hard to explain why we do not observe a strong influence of current density and pressure on the resistance in the experiments, since the gas hold-up is expected to reduce if the current density reduces or the pressure increases. Therefore, it is unlikely that the increased area resistance is solely caused by bubbles.

Although the explanations mentioned above can explain part of the observed increase in area resistance, it is likely that there

are other effects that also play a role. This can be concluded from the work of Loos [39] who has compared zero gap configurations with Zirfon diaphragms of different thickness. Our ohmic fittings (Table 3 and Table S2) show that the resistance of the thin diaphragm is $0.11 \Omega \text{ cm}^2$ lower than the thick diaphragm ($0.17 \Omega \text{ cm}^2$ vs. $0.28 \Omega \text{ cm}^2$). Although the thickness of the thinner diaphragm has not been reported, this suggests that the pure diaphragm resistance of the thick diaphragm (so excluding the effects of electrode geometry, increased gap size and bubbles) significantly exceeds $0.11 \Omega \text{ cm}^2$, since otherwise the use of a thinner diaphragm could not give such a performance improvement. Furthermore, for alkaline electrolyzers with anion-exchange membranes very low resistances of $0.1 \Omega \text{ cm}^2$ have been reported, whereas for the same electrode configuration with Zirfon a resistance of $0.3 \Omega \text{ cm}^2$ has been reported [23]. Since also for this system the effect of electrode geometry and bubbles should be comparable for the membrane and the diaphragm, this again suggests that the pure diaphragm resistance is significantly higher than $0.11 \Omega \text{ cm}^2$.

The suggestion that the resistance of the diaphragm is significantly higher than $0.11 \Omega \text{ cm}^2$ seems conflicting with the expected and experimentally observed resistances of Fig. 2, which shows resistances in the range of 0.1 to $0.15 \Omega \text{ cm}^2$ at 80°C (only the experimental value measured by Schalenbach of $0.19 \Omega \text{ cm}^2$ significantly deviates from this range [21]). The only possible explanation is that the diaphragm resistance is higher when it is in a zero gap configuration with oxygen and hydrogen evolving electrodes on both sides. This might be caused by nanobubbles.

- *Nanobubbles (adhering to the electrode, adhering to the diaphragm or inside the diaphragm).* Zirfon has small pores of $0.15 \mu\text{m}$, which is much smaller than the size of hydrogen bubbles of $\sim 20 \mu\text{m}$ [47]. Therefore, it is unlikely that hydrogen or oxygen bubbles can enter the diaphragm and block the pores. Formation of nanobubbles inside the diaphragm as a result of high local supersaturation might be a possibility, especially in the vicinity of the more hydrophobic polysulphone. However, the supersaturation or the pressure should be large (a bubble of $0.15 \mu\text{m}$ has a pressure of about 20 bar). Furthermore, if the gap size is finite, it is likely that there is a larger bubble outside the gap close to any nanobubble in the surface layer of the diaphragm. Then these nanobubbles disappear due to Ostwald ripening. Nanobubbles adhered to a solid surface, the electrode or diaphragm surface, could also be spherical cap nanobubbles. Since the curvature radius of a spherical cap nanobubble can be much larger than the size of the bubble, this bubble can be stable at relatively low supersaturation [48]. The potential role of nanobubbles requires more investigation.

For the sake of completeness we would also like to mention two other effects that could contribute to increased area resistance, yet these effects cannot explain why the thin Zirfon gives a much lower resistance than the standard Zirfon.

- *Concentration gradients.* High reaction rates can result in local gradients in KOH concentration and dissolved hydrogen and oxygen. Potentially, this could cause a concentration overpotential or local depletion of ions resulting in a lower conductivity. It has been reported that this only becomes an issue at very high current densities of $>10 \text{ A/cm}^2$ [47]. It should also result in a strong dependence of the resistance on current density, which we do not observe. However, as argued before, in regions with very high gas volume fraction, bubbles can be (nearly) stagnant, causing reduced mixing and thereby larger concentration gradients in the electrolyte.
- *Perforations completely filled with (stagnant) bubbles.* It might happen that some holes in the perforated plates are entirely

filled with stagnant gas. In that case mass transfer limitations in this hole might stop the current at the parts of the electrode surface in this hole or close to this hole.

3.5. Conclusions

Our work shows that the resistance of the Zirfon separator behaves as expected for a porous separator. Yet, resistances in zero gap alkaline electrolyzers with the Zirfon separator are significantly higher than expected based on the diaphragm resistance. Our simulations have shown that this increased resistance can partly be explained by an uneven current distribution, a finite gap and the effect of bubbles. Apart from these effects, other factors such as nanobubbles inside the diaphragm could play a role, since it seems that the diaphragm resistance is higher in the presence of gas evolving electrodes. More research into the effect of bubbles and nanobubbles is therefore clearly needed. Also, the discrepancy between our fitted resistances and the impedance measurements warrants more research.

Our review of results obtained with alkaline zero gap configurations also shows the further development potential of alkaline technology. With a thinner Zirfon type separator a potential as low as 1.72 V at 1 A/cm^2 has been achieved without using noble metals [39] and it is expected that this can be improved even further by a further optimization of the zero gap configuration and diaphragm thickness, possibly combined with a slight increase in temperature. The road to high current density alkaline electrolyzers that do not use noble metals is therefore fully open.

Declaration of Competing Interest

The authors declare that they have no known competing financial interests or personal relationships that could have appeared to influence the work reported in this paper.

Supplementary materials

Supplementary material associated with this article can be found, in the online version, at [doi:10.1016/j.electacta.2020.137684](https://doi.org/10.1016/j.electacta.2020.137684).

Credit authorship contribution statement

Matheus T. de Groot: Conceptualization, Methodology, Investigation, Writing - original draft, Writing - review & editing. **Albertus W. Vreman:** Conceptualization, Methodology, Software, Formal analysis, Writing - original draft, Writing - review & editing.

References

- [1] International Energy Agency, The Future of Hydrogen, 2019. <https://doi.org/10.1787/1e0514c4-en>.
- [2] Tractebel Engineering, Engie, Hincio, Study on Early Business Cases for H2 in Energy Storage and More Broadly Power To H2 Applications, 2017.
- [3] International Renewable Energy Agency, Hydrogen From Renewable Power: Technology outlook for the energy transition, 2018.
- [4] B.V. Tilak, P.W.T. Lu, J.E. Colman, S. Srinivasan, Electrolytic production of hydrogen, in: J.O. Bockris (Ed.), *Comprehensive Treatise of Electrochemistry*, Plenum Press, New York, 1981, pp. 1–104.
- [5] T. Grundt, K. Christiansen, Hydrogen by water electrolysis as basis for small scale ammonia production. A comparison with hydrocarbon based technologies, *Int. J. Hydrog. Energy* 7 (1982) 247–257, doi:10.1016/0360-3199(82)90088-X.
- [6] P. Vermeiren, W. Adriansens, R. Leysen, Zirfon®: a new separator for Ni-H2 batteries and alkaline fuel cells, *Int. J. Hydrog. Energy* 21 (1996) 679–684, doi:10.1016/0360-3199(95)00132-8.
- [7] G. Sandstede, R. Wurster, Water electrolysis and solar hydrogen demonstration projects, in: R.E. White (Ed.), *Modern Aspects of Electrochemistry*, Plenum Press, 1995, pp. 411–514. Number 27.
- [8] P. Vermeiren, J.P. Moreels, R. Leysen, Porosity in composite Zirfon® membranes, *J. Porous Mater.* 3 (1996) 33–40, doi:10.1007/BF01135359.

- [9] P. Vermeiren, W. Adriansens, J.P. Moreels, R. Leysen, Evaluation of the zirconium separator for use in alkaline water electrolysis and Ni-H₂ batteries, *Int. J. Hydrog. Energy* 23 (1998) 321–324, doi:10.1016/S0360-3199(97)00069-4.
- [10] Y. Sone, P. Ekdunge, D. Simonsson, Proton conductivity of Nafion 117 as measured by a four-electrode AC impedance method, *J. Electrochem. Soc.* 143 (2019) 1254–1259, doi:10.1149/1.1836625.
- [11] D. Pletcher, X. Li, S. Wang, A comparison of cathodes for zero gap alkaline water electrolyzers for hydrogen production, *Int. J. Hydrog. Energy* 37 (2012) 7429–7435, doi:10.1016/j.ijhydene.2012.02.013.
- [12] H. Wendt, V. Plzak, Electrocatalytic and thermal activation of anodic oxygen- and cathodic hydrogen-evolution in alkaline water electrolysis, *Electrochim. Acta* 28 (1983) 27–34, doi:10.1016/0013-4686(83)85083-X.
- [13] T. O'Brien, T.V. Bommaraju, F. Hine, *Handbook of Chlor-Alkali Technology*, Springer, 2005.
- [14] Asahi Kasei Chemicals Corporation, Recent Development of Asahi Kasei Chemicals' IM Technology to Reduce Power Consumption, (2009).
- [15] L. Iacopetti, Latest development in electrode coatings technology for chlor/alkali industry, in: *Proceedings of the 9th Euro Chlor International Chlorine Technology Conference and Exhibition*, 2014.
- [16] A. Scharlau, Wasserstoff-Erzeugung durch Druckelektrolyse von Wasser, Fetten, Seifen, Anstrichm. (1960) 185–189.
- [17] R. Phillips, A. Edwards, B. Rome, D.R. Jones, C.W. Dunnill, Minimising the ohmic resistance of an alkaline electrolysis cell through effective cell design, *Int. J. Hydrog. Energy* 42 (2017) 23986–23994, doi:10.1016/j.ijhydene.2017.07.184.
- [18] N. Nagai, M. Takeuchi, T. Kimura, T. Oka, Existence of optimum space between electrodes on hydrogen production by water electrolysis, *Int. J. Hydrog. Energy* 28 (2003) 35–41, doi:10.1016/S0360-3199(02)00027-7.
- [19] R.L. LeRoy, Industrial water electrolysis: present and future, *Int. J. Hydrog. Energy* 8 (1983) 401–417, doi:10.1016/0360-3199(83)90162-3.
- [20] W. Ju, M.V.F. Heinzl, L. Pusterla, M. Hofer, B. Fumey, R. Castiglioni, M. Pagani, C. Battaglia, U.F. Vogt, Lab-scale alkaline water electrolyzer for bridging material fundamentals with realistic operation, *ACS Sustain. Chem. Eng.* 6 (2018) 4829–4837, doi:10.1021/acssuschemeng.7b04173.
- [21] M. Schalenbach, G. Tjarks, M. Carmo, W. Lueke, M. Mueller, D. Stolten, Acidic or alkaline? Towards a new perspective on the efficiency of water electrolysis, *J. Electrochem. Soc.* 163 (2016) F3197–F3208, doi:10.1149/2.0271611jes.
- [22] M.R. Kraglund, M. Carmo, G. Schiller, S.A. Ansar, D. Aili, E. Christensen, J.O. Jensen, Ion-solvating membranes as a new approach towards high rate alkaline electrolyzers, *Energy Environ. Sci.* 12 (2019) 3313–3318, doi:10.1039/c9ee00832b.
- [23] M.R. Kraglund, E. Christensen, Alkaline Membrane Water Electrolysis With Non-Noble Catalysts, Technical University of Denmark, 2017 www.energy.dtu.dk.
- [24] F. Baumgart, A. Brinner, B. Feigl, V. Kindl, U. Lenz, P. Sichler, S. Steiert, Verbundprojekt "P2G-Elektrolyse" Öffentlicher Schlussbericht ZSW-Teilvorhaben FKZ 0325524A, 2017.
- [25] J.R. Bowen, J.J. Brentzen, P.S. Jørgensen, W. Zhang, RES Hydrogen: Efficient Pressurised Alkaline Electrolyzers, 2014.
- [26] R.B. MacMullin, G.A. Muccini, Characteristics of porous beds and structures, *AIChE J.* 2 (1956) 393–403, doi:10.1002/aic.690020320.
- [27] B. Tjaden, D.J.L. Brett, P.R. Shearing, Tortuosity in electrochemical devices: a review of calculation approaches, *Int. Mater. Rev.* 63 (2018) 47–67, doi:10.1080/09506608.2016.1249995.
- [28] R. Coquet, ZIRFON PERL™ Separator for Alkaline Water Electrolysis. Hann. Messe, 2016.
- [29] P. Aerts, S. Kuypers, I. Genné, R. Leysen, J. Mewis, I.F.J. Vankeulecom, P.A. Jacobs, Polysulfone – ZrO₂ surface interactions. The influence on formation, morphology and properties of zirconium-membranes, *J. Phys. Chem. B* 110 (2006) 7425–7430, doi:10.1021/jp053976c.
- [30] M.J. Martínez, S. Shimpalee, J.W. Van Zee, Measurement of MacMullin numbers for PEMFC gas-diffusion media, *J. Electrochem. Soc.* 156 (2009) B80, doi:10.1149/1.3005564.
- [31] B. Tjaden, S.J. Cooper, D.J. Brett, D. Kramer, P.R. Shearing, On the origin and application of the Bruggeman correlation for analysing transport phenomena in electrochemical systems, *Curr. Opin. Chem. Eng.* 12 (2016) 44–51, doi:10.1016/j.coche.2016.02.006.
- [32] R.J. Gilliam, J.W. Graydon, D.W. Kirk, S.J. Thorpe, A review of specific conductivities of potassium hydroxide solutions for various concentrations and temperatures, *Int. J. Hydrog. Energy* 32 (2007) 359–364, doi:10.1016/j.ijhydene.2006.10.062.
- [33] Z. Li, K.S. Pitzer, Thermodynamics of aqueous KOH over the full range to saturation and to 573 K, *J. Solut. Chem.* 25 (1996) 813–823, doi:10.1007/BF00972574.
- [34] J. Dukovic, C.W. Tobias, The Influence of Attached Bubbles on Potential Drop and Current Distribution at Gas-Evolving Electrodes, 1987.
- [35] K. Aoki, Y. Nishiki, Computation of primary current distribution and cell resistance at model electrodes with circular perforations, *J. Appl. Electrochem.* 19 (1989) 183–187, doi:10.1007/BF01062298.
- [36] V. Kienzlen, D. Haaf, W. Schnurnberger, Location of hydrogen gas evolution on perforated plate electrodes in zero gap cells, *Int. J. Hydrog. Energy* 19 (1994) 729–732, doi:10.1016/0360-3199(94)90235-6.
- [37] J. Rodríguez, S. Palmas, M. Sánchez-Molina, E. Amores, L. Mais, R. Campana, Simple and precise approach for determination of Ohmic contribution of diaphragms in alkaline water electrolysis, *Membranes* 9 (2019), doi:10.3390/membranes9100129.
- [38] U.R. Fischer, A. Voigt, D. Tannert, H.J. Krautz, Pressure and temperature influence on alkaline water electrolysis performance, in: *Proceedings of the European PEFC H₂ Forum*, 2015.
- [39] S. Loos, Active anodes for alkaline water electrolysis. *Advanced Alkaline Electrolysis*, 3rd Ind. Work., 2020.
- [40] W.C. Kincaide, Technical developments in alkaline water electrolysis, in: *Proceedings of the International Symposium on Advanced Hydrogen Manufacturing, Las Vegas, 1982*, p. 37.
- [41] Ø. Ulleberg, Modeling of advanced alkaline electrolyzers: a system simulation approach, *Int. J. Hydrog. Energy* 28 (2003) 21–33, www.elsevier.com/locate/ijhydene.
- [42] H. Barthels, W.A. Brocke, K. Bonhoff, H.G. Groehn, G. Heuts, M. Lennartz, H. Mai, J. Mergel, L. Schmid, P. Ritzenhoff, PHOEBUS-Jülich: an autonomous energy supply system comprising photovoltaics, electrolytic hydrogen, fuel cell, *Int. J. Hydrog. Energy* 23 (1998) 295–301, doi:10.1016/S0360-3199(97)00055-4.
- [43] G. Schiller, R. Henne, P. Mohr, V. Peinecke, High performance electrodes for an advanced intermittently operated 10-kW alkaline water electrolyzer, *Int. J. Hydrog. Energy* 23 (1998) 761–765.
- [44] M. Schalenbach, O. Kasian, K.J.J. Mayrhofer, An alkaline water electrolyzer with nickel electrodes enables efficient high current density operation, *Int. J. Hydrog. Energy* 43 (2018) 11932–11938, doi:10.1016/j.ijhydene.2018.04.219.
- [45] F. Hernandez-Alvarado, D.V. Kalaga, D. Turney, S. Banerjee, J.B. Joshi, M. Kawaji, Void fraction, bubble size and interfacial area measurements in co-current downflow bubble column reactor with microbubble dispersion, *Chem. Eng. Sci.* 168 (2017) 403–413, doi:10.1016/j.ces.2017.05.006.
- [46] P. Haug, B. Kreitz, M. Koj, T. Turek, Process modelling of an alkaline water electrolyzer, *Int. J. Hydrog. Energy* 42 (2017) 15689–15707, doi:10.1016/j.ijhydene.2017.05.031.
- [47] C.W.M.P. Sillen, E. Barendrecht, L.J.J. Janssen, S.J.D. van Stralen, Gas bubble behaviour during water electrolysis, *Int. J. Hydrog. Energy* 7 (1982) 577–587, doi:10.1016/0360-3199(82)90038-6.
- [48] D. Lohse, X. Zhang, Surface nanobubbles and nanodroplets, *Rev. Mod. Phys.* 87 (2015) 981–1035, doi:10.1103/RevModPhys.87.981.
- [49] Agfa, Technical Data Sheet ZIRFON PERL UTP 500, (2020).
- [50] H.I. Lee, M. Mehdi, S.K. Kim, H.S. Cho, M.J. Kim, W.C. Cho, Y.W. Rhee, C.H. Kim, Advanced Zirconium-type porous separator for a high-rate alkaline electrolyser operating in a dynamic mode, *J. Memb. Sci.* 616 (2020) 118541, doi:10.1016/j.memsci.2020.118541.